

SDE: Early Screening for Dry Eye Disease with Wireless Signals

MENG XUE[§], Hong Kong University of Science and Technology, China

YUYANG ZENG[§], Eye Center, Wuhan University Renmin Hospital, China

SHENGKANG GU, Wuhan University, China

QIAN ZHANG*, Hong Kong University of Science and Technology, China

BOWEI TIAN, Wuhan University, China

CHANGZHENG CHEN*, Eye Center, Wuhan University Renmin Hospital, China

Early screening for dry eye disease (DED) is crucial to identify and provide timely intervention to high-risk susceptible populations. Currently, clinical methods for diagnosing DED include the tear break-up time test, meibomian gland analysis, tear osmolarity test, and tear river height test, which require in-hospital detection. Unfortunately, there is no convenient way to screen for DED yet. In this paper, we propose *SDE*, a contactless, convenient, and ubiquitous DED screening system based on RF signals. To extract biomarkers for early screening of DED from RF signals, we construct frame chirps variance and extract fine-grained spontaneous blinking action. *SDE* is carefully designed to remove interference in RF signals and refine the characterization of biomarkers that denote the symptoms of DED. To endow *SDE* with the ability to adapt to new users, we develop a deep learning-based model of unsupervised domain adaptation to remove the influence of different users and environments in local and global two-level feature spaces. We conduct extensive experiments to evaluate *SDE* with 54 volunteers in 4 scenes. The experimental results confirm that *SDE* can accurately screen for DED in a new user in real environments such as eye examination rooms, clinics, offices, and homes.

CCS Concepts: • Human-centered computing → Ubiquitous and mobile computing.

Additional Key Words and Phrases: Dry eye disease, spontaneous blinking, biomarker, mmWave sensing

ACM Reference Format:

Meng Xue[§], Yuyang Zeng[§], Shengkang Gu, Qian Zhang*, Bowei Tian, and Changzheng Chen*. 2023. *SDE: Early Screening for Dry Eye Disease with Wireless Signals*. 1, 1 (October 2023), 23 pages. <https://doi.org/10.1145/nnnnnnn.nnnnnnn>

1 INTRODUCTION

A meta-analysis of three studies [25] shows that the prevalence of dry eye disease (DED) in the United States is 8.1%. According to a global epidemiological study [31], the incidence of DED varies from 5% to 50%. Unfortunately, with the advancement of technology and the widespread use of electronic devices such as smartphones, tablets, and computers, the incidence of DED is increasing annually. Furthermore, DED is a chronic disease that typically requires long-term treatment. However, patients with mild dry eye often have a poor prognosis due to the lack of

[§]Both authors contributed equally to this research.

*Corresponding authors.

Authors' addresses: Meng Xue[§], csexuemeng@ust.hk, Hong Kong University of Science and Technology, China; Yuyang Zeng[§], yuyangz@whu.edu.cn, Eye Center, Wuhan University Renmin Hospital, China; Shengkang Gu, gushengkang@whu.edu.cn, Wuhan University, China; Qian Zhang*, qianzh@cse.ust.hk, Hong Kong University of Science and Technology, China; Bowei Tian, boweitian@whu.edu.cn, Wuhan University, China; Changzheng Chen*, whuchenzh@163.com, Eye Center, Wuhan University Renmin Hospital, China.

Permission to make digital or hard copies of all or part of this work for personal or classroom use is granted without fee provided that copies are not made or distributed for profit or commercial advantage and that copies bear this notice and the full citation on the first page. Copyrights for components of this work owned by others than ACM must be honored. Abstracting with credit is permitted. To copy otherwise, or republish, to post on servers or to redistribute to lists, requires prior specific permission and/or a fee. Request permissions from permissions@acm.org.

© 2023 Association for Computing Machinery.

XXXX-XXXX/2023/10-ART \$15.00

<https://doi.org/10.1145/nnnnnnn.nnnnnnn>

obvious early symptoms, neglect of symptoms, and untimely medical treatment [39]. Therefore, early screening of DED is crucial for high-risk susceptible populations to prevent the permanent and irreversible deterioration of dry eye.

Several clinical tests are commonly used for diagnosing Dry Eye Disease (DED), including the Ocular Surface Disease Index (OSDI) [29], Schirmer's Test (ST) [32], Tear Break-Up Time (TBUT) [7], Meibomian Gland Analysis (MGA) [9, 30], Tear Osmolarity [11], and Tear River Height (TRH) [24]. However, these clinical tests require patients to visit hospitals for designated testing, which can be expensive, invasive, and untimely. To address these issues, various researchers have attempted to develop contactless and automated methods for detecting DED. For example, Hong et al. [19] developed a screening method using a smartphone to capture images of the eyes, achieving 75% accuracy in identifying mild DED. However, there is currently no DED screening method that is contactless, convenient, and ubiquitous, which could greatly benefit early detection and timely intervention.

In marked contrast to existing methods for screening DED, in this paper, we explore biomarkers of DED by using RF signals to achieve contactless, convenient, and ubiquitous DED screening. Similar to the Google Nest Hub (2nd gen) [3], which provides personalized tips to improve sleep and overall health using the Soli radar [4], our system, *SDE*, uses RF signals to achieve contactless, convenient, and ubiquitous DED screening. *SDE* does not require invasive inspections or hospital visits, making it suitable for early screening of DED at home, which is both convenient and user-friendly. Table 1 demonstrates a comparison of sensing modalities for detecting DED. Compared to existing minute motion sensing modalities, RF goes further that enables to capture blink dynamics, which is attributed to its highly precise perception with a granularity as low as 60us. In addition, RF does not exist lightness disturbance and privacy concerns with regards to vision-based methods.

To realize an RF-based DED early screening system, several challenges need to be addressed.

- *How to extract spontaneous blinking action from RF signals that contain DED biomarkers?*

Although several studies have focused on activity detection using RF signals, no prior research has explored RF-based DED screening approaches. It is challenging to extract fine-grained spontaneous blinking action containing DED biomarkers.

- *How to eliminate interferences in the spontaneous blinking action and refine feature profiles?*

RF signals are susceptible to multipath interference from the surrounding environment, including stationary and moving objects. It is crucial to eliminate these interferences to effectively extract spontaneous blinking action.

- *How to establish an effective and robust DED screening model that can adapt to new users?*

Since spontaneous blinking occurs involuntarily, like breathing, it is essential to remove the influence of different users and environments to enable the system to adapt to new users effectively.

To tackle these challenges, we propose *SDE*, an RF-based DED screening system that uses commercial off-the-shelf (COTS) radar devices. *SDE* comprises three main components, i.e., frame chirps variance (FCV) construction, DED biomarker extraction, and deep learning-based DED screening. To capture fine-grained spontaneous blinking through RF signals, we first locate the user's head position to remove interference from the environment. We then construct FCV by utilizing variances of a frame chirp based on amplitude information in the frequency bin at the head position. To extract biomarkers of DED, we design a series of signal processing algorithms to refine FCV. After this, we leverage Fourier synchrosqueezed transform (FSST) [26] to obtain a clear spontaneous blinking feature profile that contains biomarkers of DED. To empower *SDE* with the ability to adapt to new users, we utilize a deep learning-based unsupervised domain adaptation (UDA) model to remove interference from different users and environments in both local and global feature spaces.

We conduct extensive experiments to evaluate *SDE* with 54 volunteers in 4 scenes. The experiment results confirm that *SDE* can accurately screen for DED in new users in real-world environment, achieving an average screening accuracy of 94.22% across four scenarios, i.e., eye examination rooms, clinics, offices, and homes.

We highlight our key contributions as follows.

Table 1. A comparison of sensing modalities for DED screening.

Method	Range	Sensing modality	Granularity	Privacy
[21]	50-90cm	Ultrasonic	40ms	✓
[6]	3-5cm	Infrared sensor	50ms	✓
[13]	30-60cm	Camera	30fps: 33ms 120fps: 8ms	✗
<i>SDE</i>	15-50cm	RF	60us	✓

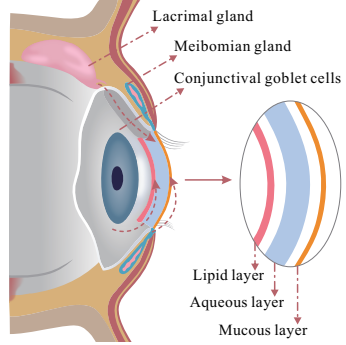


Fig. 1. The structure of a tear film.

- To the best of our knowledge, we are the first to investigate the feasibility of using RF signals for screening dry eye disease and realize a contactless, ubiquitous, and convenient system called *SDE*. To extract biomarkers of DED for screening, we construct FCV by utilizing variances of a frame chirps based on amplitude information in the frequency bin at the head position, achieving the extraction of fine-grained spontaneous blinking.
- We design a series of sophisticated algorithms to eliminate interference in RF signals and refine the characterization of biomarkers that denote the symptoms of DED.
- To endow *SDE* with the ability of adapting to new users, we leverage a deep learning-based unsupervised domain adaptation model to remove the influence of different users and environments in both local and global feature spaces.
- We implement and conduct extensive experiments on *SDE* in real-world environments. The results demonstrate that *SDE* can accurately screen for dry eye disease with high accuracy.

2 BACKGROUND AND PRELIMINARIES

2.1 Dry Eye Disease

DED is a complex ocular surface disease characterized by a loss of tear film homeostasis, leading to symptoms of visual dysfunction, discomfort, and tear film instability, accompanied by hyperosmolarity and ocular surface inflammation and damage [39]. The tear film is generated by a lacrimal gland, which is located superior temporally to each eye and behind the upper eyelid. The lacrimal gland secretes lacrimal fluid that flows into the space between the eyeball and eyelid through the excretory ducts, and it spreads across the eye surface with each blink. The lacrimal fluid gathers in the lacrimal lake and is drawn into the puncta by capillary action before flowing into the nasal cavity through the lacrimal canaliculi at the inner corner of the eyelids.

As shown in Fig. 1, the tear film coating the eye consists of three distinct layers. **Lipid layer** mainly comprising oils secreted by the meibomian glands, retards the water evaporation of the aqueous layer. **Aqueous layer** primarily composed of water with a small amount of salt, spreads the tear film, regulates osmotic pressure, and controls infectious agents. **Mucous core** consisting of mucin secreted by the conjunctival goblet cells, stabilizes the tear film and prevents bacterial dust from adhering to the ocular surface.

The causes of DED are widespread and complex [5]. Allergies, environmental factors (such as dust, wind, heat, and dryness), hormonal changes associated with aging and pregnancy, numerous diseases, and medications can all contribute to DED. Additionally, the use of contact lenses and smart screens can cause dry eye syndrome, which is increasingly prevalent. As the pathogenesis of DED is still unclear, symptomatic treatment measures such

as topical medication and physical therapy are commonly used clinically. Symptoms of DED include subjective sensations such as dryness, foreign body sensation, burning sensation, fatigue, discomfort, and vision fluctuations, as well as objective signs such as decreased tear secretion and increased blinking. However, unique eye blink characteristics of DED have not yet been fully understood.

2.2 Spontaneous Blinking in Dry Eye Disease

The maintenance of a stable tear film over the ocular surface relies not only on tear secretion and lipid quality, but also on the essential role of spontaneous blinking. Unlike reflex and voluntary blinks, spontaneous blinks are rapid, automatic, and unconscious movements of the eyelids that facilitate tear film spreading, including lipid secretion and tear drainage. Furthermore, spontaneous blinking can affect the optical quality of the eye [34].

However, the high speed of spontaneous blinking (less than 100 ms) [34] makes it challenging to investigate its characteristics. Previous studies have mainly focused on blink rate and interblink interval (IBI) as the main parameters for evaluating spontaneous blinks in DED [27, 39]. Nevertheless, these parameters only provide means and variances and fail to describe the continuous dynamic change in the spontaneous blinking process. Therefore, understanding the relationship between DED and blinking requires the analysis of more complex blink patterns. Recent studies [20, 34, 45] have identified incomplete blinks, short blink intervals, and prolonged eyelid closed time as key characteristics of spontaneous blinking in DED. Incomplete blinking, in particular, has been linked to increased meibomian gland dropout (MGD), decreased tear breakup time (TBUT), and increased ocular surface disease index (OSDI) [20]. Consequently, it has been suggested that incomplete blinking frequency could be an indicator of DED severity [45]. To investigate biomarkers of DED, it is crucial to extract fine-grained spontaneous blinking action from RF signals.

2.3 Biomarkers of DED Using FCV

We visualize unique characteristics of spontaneous blinking between normal individuals and DED patients using FCV (details of construction in Section 3.3).

Fig. 2 demonstrates the spontaneous blinking action based on FCV from normal individuals (N-) and DED patients (P-) when seated 30cm in front of the radar. As shown in Fig. 2, we can observe that spontaneous blinking habits vary among different person. By comparing Fig. 2(f) and Fig. 2(m), we can observe that DED patients have a higher blink frequency, while by comparing Fig. 2(a) and Fig. 2(j), we observe that DED patients have a lower blink frequency. Therefore, the eye blink frequency is not a robust enough screening measure for DED.

To investigate the characteristics of spontaneous blinking further, we delve into the unique feature patterns of spontaneous blinking. Based on the DED patient group, we can observe that spontaneous blinking action has several biomarkers, including higher frequency in incomplete blinking, continuous blink, and continuous incomplete blinking. These observations are consistent with recent research on incomplete blinking frequency's association with DED [45]. Fig. 2(m) and Fig. 2(k) demonstrate five and two incomplete blinks, respectively, in the DED patient group, while there is no incomplete blink in Fig. 2(c) in the normal group. As shown in Fig. 2(i), due to tear film instability, DED patients often require more consecutive blinks to protect the iris. Moreover, Fig. 2(l) shows that DED patients have longer blink intervals and three-continuous blinks.

To assess the robustness of these biomarkers under time-varying conditions, we further investigate their consistency over time. Since spontaneous blinking is not consistent over time, assessing the robustness of these biomarkers under time-varying conditions is crucial for DED screening. Fig. 3 illustrates that spontaneous blinking action varies over time in both normal individuals and DED patients, but the biomarkers of higher frequency in incomplete blinking, continuous blink, and continuous incomplete blinking still exist. Therefore, these biomarkers are robust for DED screening.

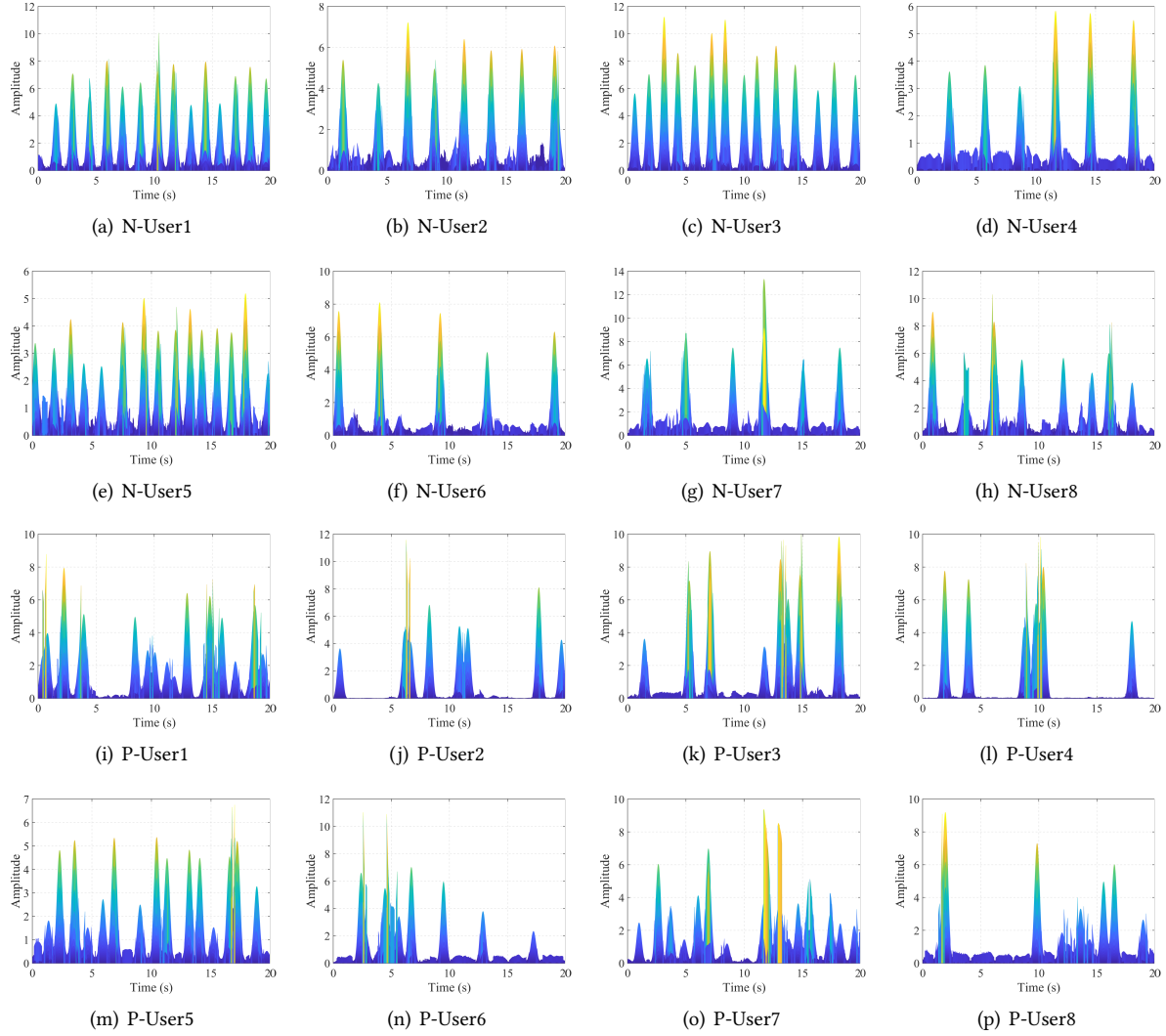


Fig. 2. The spontaneous blinking action among different users, including both normal individual (N-) and DED patient (P-). Note that the spontaneous blinking varies between individuals. However, DED patients exhibit a unique feature pattern.

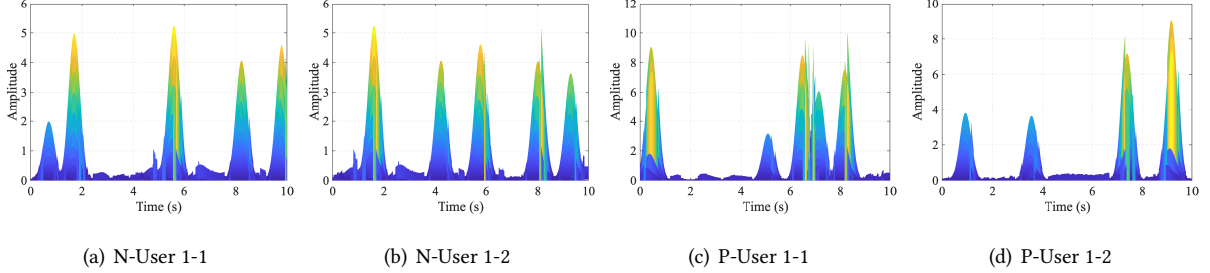


Fig. 3. The spontaneous blinking action at different times in both normal individuals and those with DED. Note that the spontaneous blinking varies over time.

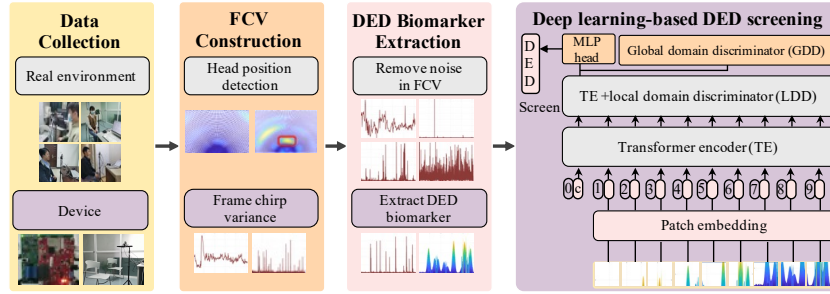


Fig. 4. System framework of SDE.

2.4 Challenges

To materialize a contactless and ubiquitous RF-based DED screening system, we need to resolve the following challenges.

- **Extracting fine-grained spontaneous blinking action.** One of the main obstacles is the limited resolution of off-the-shelf radar [2], making it difficult to obtain the required fine-grained spontaneous blinking action. To tackle this problem, we first identify user's head position to eliminate noise outside the range of uses. We then construct FCV by leveraging variances of a frame chirps based on amplitude information in the frequency bin at the head position.
- **Refining biomarkers profiles.** Wireless signals have the inherent characteristic of multipath reflection, and the construction of FCV while deriving fine-grained spontaneous blinking may introduce noise. It is essential to refine biomarkers profiles for DED screening. To resolve this problem, we first design a series of signal processing algorithms to denoise, i.e., noise introduced by head movement, noise caused by FCV, and other entwined non-linear interference.
- **Screening DED for a new person.** Spontaneous blinking happens without conscious effort. Furthermore, the FCV may be influenced by different real environments. To empower SDE to adapt to new users, we utilize a deep learning-based UDA model to remove the influence of different users and environments in local and global two-level feature spaces.

3 EARLY SCREENING FOR DRY EYE DISEASE

3.1 Overview

As illustrated in Fig. 4, SDE comprises four main modules, i.e., data collection, FCV construction, DED biomarker extraction, and deep learning-based DED screening.

- *Data collection.* We leverage a commercial radar to realize a contactless, and ubiquitous DED screening system.
- *FCV construction.* We search user's head position, and construct FCV by using the reflected RF signals from human eyes in the radar's field of view (FOV).
- *DED biomarker extraction.* We design a series of algorithms to remove noise in FCV, and extract DED biomarkers profile by employing Fourier synchrosqueezed transform.
- *Deep learning-based DED screening.* We design a deep learning-based UDA model to conduct early screening for DED for new users.

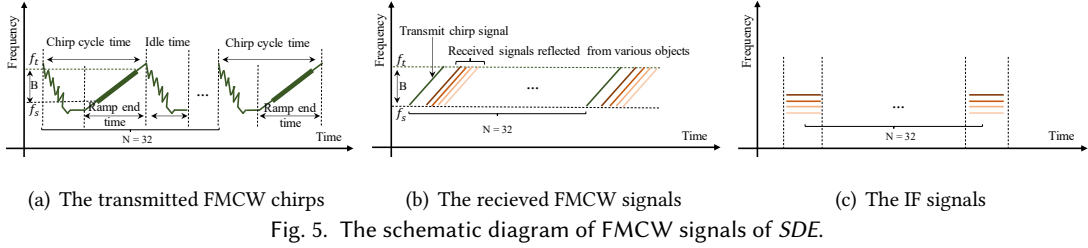


Fig. 5. The schematic diagram of FMCW signals of SDE.

3.2 Data Collection

We employ an off-the-shelf (COTS) mmWave radar [2] to transmit frequency-modulated continuous wave (FMCW) signals. The radar device costs \$299 with the core chip accounting for \$40. The bounced RF signals are received by the COTS radar and then treamed to a computer by COTS DCA1000EVM [1]. The FMCW signal operates in the frequency range of 77Ghz to 81Ghz, resulting in a wavelength of 4mm. We use two antennas for transmission and four antennas for reception of the wireless signals. The radar's field of view (FOV) is set to 30° in the vertical and 120° in the horizontal direction. Each FMCW chirp consists 512 data samples, and the slope is 29.982Mhz/us, with an analog-to-digital converter (ADC) sampling rate of 10,000k/s. Based on the slope and ADC sampling rate, the max sensing distance of the device can be calculated by:

$$Dis = \frac{S_{adc} \times c}{2 \times S}, \quad (1)$$

where S_{adc} , S , and c , denote the ADC sampling rate, the slope, and the speed of light, respectively. We can estimate the maximum sensing distance to be approximately 50m using Eq. 1. We set the ramp end time for each chirp to 60us, with an idle time of 100us for each chirp.

3.3 FCV Construction

In this section, we describe how to construct a frame chirps variance (FCV) from FMCW signals bounced from a person.

3.3.1 Removing Noise of Multi-path. As depicted in Fig. 5(a), we utilize the device to transmit FMCW signals, which contain a group of chirps. During the ramp end time, also known as the sweep time, the frequency of chirp signals increases linearly with time. Specifically, we denote the frequency of chirp signals as $f(t) = f_s + \frac{B}{2T}t$, where f_s , B , and T denote the initial frequency, sweep bandwidth, and sweep time, respectively. Therefore, we can denote the transmitted chirp signals in the time domain as:

$$S(t) = \exp(-j2\pi f(t)t), \quad (2)$$

where $f(t)$ is the frequency of chirp signals. As shown in Fig. 5(b), we denote the received signals in realistic environments as:

$$R(t) = \sum_{i=1}^M A_i \exp(-j2\pi f(t - \tau_i)(t - \tau_i)), \quad (3)$$

where A_i , M , τ_i denote the attenuation, number of multi-path, and time-of-flight of the i -th path. As shown in Fig. 5(c), by multiplying $S(t)$ and $R(t)$ and filtering out the first high-frequency term, we can denote the intermediate frequency (IF) signal as:

$$IF(t) = \sum_{i=1}^M A_i \exp\left(-j2\pi(f_s\tau_i - \frac{B(\tau_i^2 - 2t\tau_i)}{2T})\right). \quad (4)$$

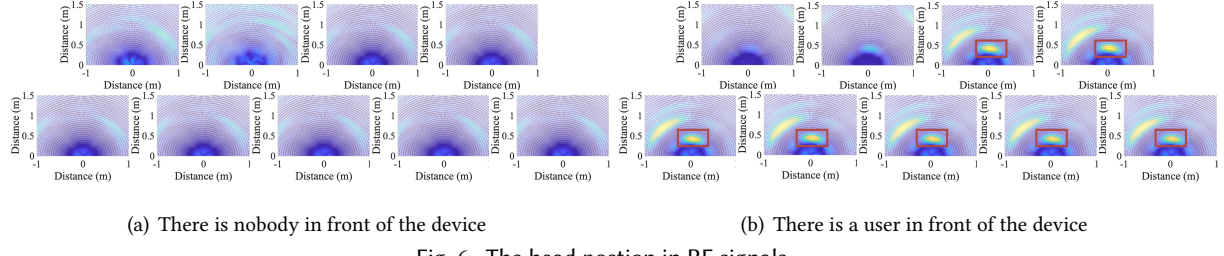


Fig. 6. The head position in RF signals.

ALGORITHM 1: Searching the head position based on speed and reflection strength.

Input: Intermediate frequency signal $IF(t)$, number of chirps per frame $n_{chirps} = 32$, Range FFT size $N = 1024$, Doppler FFT size $M = 249$, Angle FFT size $Q = 180$.

Output: Head position.

- 1 **Phase 1:** Compute 3-dimension FFT on $IF(t)$ to extract distance, speed, and angle information.
- 2 A window size of 256 for range FFT.
- 3 Calculate range FFT based on $IF(t)$ to obtain $RangeP(t) = FFT(IF(t), N)$.
- 4 The window size for dopper FFT is $n_{chirps} = 32$.
- 5 Calculate dopper FFT based on $RangeP(t)$ to obtain $DopplerP(t) = FFT(RangeP(t), M)$.
- 6 Calculate angle FFT based on $DopplerP(t)$ to obtain $AngleP(t) = FFT(DopplerP(t), Q)$.
- 7 **Phase 2:** Search for head center postion in distance and angle dimension.
- 8 Get the potential head area $HeadP_{S1} = AngleP(N, S[0 : 8], Q)$.
- 9 **while** $i \leftarrow 0$ to $S = 8$ **do**
- 10 Compute the maximum reflection strength $MaxR = HeadP_{S_i} = AngleP(N, S_i, Q)$.
- 11 Split $HeadP_{S_i}$ in the first dimension by 8 into $HeadP_{S2} = AngleP(N[0 : N/8], Q)$.
- 12 Head position set $HeadPSet$.
- 13 **for** $k \leftarrow 1$ to $K = N/8$ **do**
- 14 Compute the point with the max reflection strength $Maxr = HeadP_{S2}(x_k, y_k)$.
- 15 The potential border of head: $xr_{border} = round(3/y_k \times 180/\pi) + x_k$;
 $xf_{border} = x_k - round(3/y_k \times 180/\pi)$.
- 16 **if** $(Maxr \geq 0.7 \times MaxR) \&& (AngleP(xr_{border}, y_k) \leq 0.2 \times Maxr ||$
 $AngleP(xf_{border}, y_k) \leq 0.2 \times Maxr)$ **then**
- 17 Add this point (x_k, y_k) to $HeadPSet$.
- 18 Remove the point that is outside the radar's FOV.
- 19 **end**
- 20 **end**
- 21 Find the max reflection strength in $HeadPSet$ as the head center position (x_h, y_h) of $AngleP(N, S_i, Q)$.
- 22 **end**
- 23 Output the head position (x_h, y_h) by calculating the mode of the nine head center positions.

To eliminate the interference caused by multi-path, we use Algorithm 1 to locate the head position of users based on velocity and reflection intensity information in the $IF(t)$ signal. On one hand, users have various vital

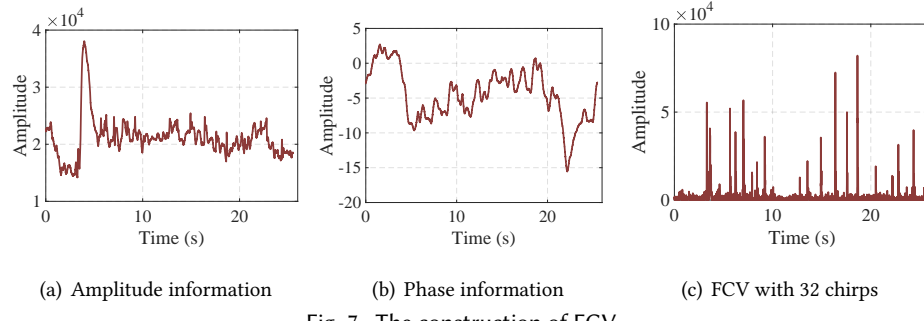


Fig. 7. The construction of FCV.

signs, such as breathing and heartbeat, which cause them to constantly move. Therefore, the velocity in the $IF(t)$ signal can be used as a marker to filter out the noise rebounded from static objects. On the other hand, since the user is closest to the device, signals reflected from the user have the strongest reflection strength. Hence, the reflection intensity information in the $IF(t)$ signal can also be used as a marker to filter out the noise rebounded from other objects.

The algorithm consists of two phases, i.e., *compute 3-dimension FFT on IF(t) to extract distance, speed, and angle information* and *search for head center position in distance and angle dimension*. In the first phase, we compute a 3D FFT to obtain range, doppler, and angle information, as described in lines 2-6. Since users sit in front of the SED, allowing for locating the head through relative stillness. In line 8, we utilize $S[0 : 8]$ to reduce computational load, where $S[0]$ represents static and $S[8]$ denotes the max speeds of head movement. Then, we compute the maximum reflection strength on this velocity, denoting it as the distance and angle in line 10. Since each frequency bin represents information around 5 cm (based on the maximum sensing distance of 50 m and 1024 range FFT points), we divide the distance into intervals of 40 cm and create 128 sub-areas by $N[0 : N/8]$ in line 11.

After this, we search for the head point among these 128 sub-areas in line 13-20. Specifically, in line 14, we first detect the potential head position by identifying the strongest reflection intensity within each sub-area. Then, we determine the potential head border by its shape and the reflection at the head border is weaker compared to the center in lines 15-16, whose threshold is empirical determined. In addition, we remove candidate head center points that are outside the radar's FOV in line 18. Finally, we extract the head position by finding the maximum reflection strength at each velocity in line 21 and output the head position by computing the mode of the nine head center positions at all velocities in line 23.

3.3.2 Constructing FCV. After eliminating the noise caused by multi-path, the challenge of depicting spontaneous blinking action using RF signals needs to be addressed.

As shown in Fig. 7(b), the phase information of the received signals in the frequency bin at the head position is highly disordered due to its sensitivity to small motion, which results in excessive responses to the noise present in realistic environments. This indicates that the phase information has weak anti-interference ability. As illustrated in Fig. 7(a), the amplitude information of the signals in the frequency bin at the head position is also sensitive to small motion, making it possible to extract fine-grained spontaneous blinking. Moreover, the amplitude information can respond substantially to spontaneous blinking, demonstrating better anti-interference ability than the phase information. However, the fine-grained spontaneous blinking action still appears blurry in the amplitude information, making it challenging to extract this action.

To overcome this problem, we propose constructing a frame chirps variance representation based on the amplitude information derived from the frequency bin at the head position. Since the amplitude information in a single chirp appears disordered, we expand the observation window to serve as a special filter. This window size determines the sensitivity of RF signals to spontaneous blinking actions. Specifically, the sensitivity of RF signals

decreases as the window size increases. Fig. 7(a) shows that many noises are present when the window size is short. However, the amplitude information cannot capture the spontaneous blinking motion when the windows size is too large. Therefore, we construct the FCV representation as follows:

$$FCV = \sum_{n=1}^N V\{|FFT(RF_n)|\}, \text{ where } V(\cdot) = \frac{\sum_{i=1}^n (x_i - \bar{x})^2}{n}, \quad (5)$$

where RF_n represents the amplitude information of signals in the frequency bin at the head position in the short time window, and N denotes the window size, $V(\cdot)$ denotes the sensitivity metric in the window. The variance $V(\cdot)$ calculates the degree of amplitude value change in the window, and FCV is an accumulated variance in a short time window, representing how the RF signals change at the time of blinking. The degree of change of this value reflects the state of eye movement at different times. We set N to be 32 empirically, resulting in the short time window to be $32 \times 160\mu s = 5.12ms$. As shown in Fig. 7(c), the FCV profile can effectively capture the fine-grained spontaneous blinking action.

3.4 DED Biomarker Extraction

After obtaining the FCV from FMCW signals, the next challenge is to extract an effective pattern of DED from the FCV. To overcome this challenge, the first step is to denoise the spontaneous blinking action in the FCV. This involves removing noise introduced by head movement, noise caused by FCV construction, and other non-linear interference that may be entwined with the signal. Once the FCV has been denoised, we extract the pattern of DED using the FSST, which contains biomarkers of DED.

3.4.1 Denoising for Spontaneous Blinking Action. To extract an effective dry eye disease pattern, it is necessary to remove noise from the FCV profiles, including those caused by head movement and FCV construction, as well as other entwined non-linear interference. First of all, we normalize the amplitude of the FCV profile to reduce the adverse effects of singular data points. Although we use variance as the sensitivity metric in the window during FCV construction, this can introduce variance noise that may obscure the spontaneous blink action after normalization, as shown in Fig. 8(b). For instance, in the amplitude information shown in Fig. 8(a), the local kurtosis is extremely large even though there is no spontaneous blink action, which can lead to an isolated large peak in the FCV profile. To remove these instantaneous spikes, we apply two filters, namely Hampel and rmoutliers. The Hampel filter can be denoted as follows:

$$|FCV_i - \text{md}(FCV_i, L)| > \delta \times \text{std}(FCV_i, L), \quad (6)$$

where $\text{md}(FCV_i, L)$, $\text{std}(FCV_i, L)$, L , and δ denote the median, standard deviation, a local window composed of the FCV_i sample and its surrounding samples, and the threshold, respectively. We replace a detected outlier FCV_i with $\text{md}(FCV_i, L)$. The rmoutliers filter can be denoted as follows:

$$FCV_i - \text{md}(FCV_i) > \eta \times \text{md}(\|FCV_i - \text{md}(FCV)\|), \quad (7)$$

where η denotes the percentile threshold. We set η to be 99.5%, resulting in any data point that exceeds the 99.5% threshold being regarded as an outlier and replaced with half of the mean. As shown in Fig. 8(c), these two filters can effectively eliminate the variance noise of instantaneous spikes.

Another source of disturbance is involuntary head movements, which are difficult to avoid and can introduce noise in the FCV profiles. This noise is often larger than that caused by spontaneous blinking actions, making it hard to eliminate by simply reducing the sensitivity of FCV profiles. As shown in Fig. 9(a), we can see that head shaking results in a group of peaks that represent noise and can be removed based on FCV signal density. Specifically, we identify all peaks in a window of $L_p = 61$ points ($61 \times (160\mu s \times 32) = 312.32ms$) in the FCV profiles, where the difference between two adjacent peaks must be larger than $3 \times \text{mean}(FCV)$. We remove

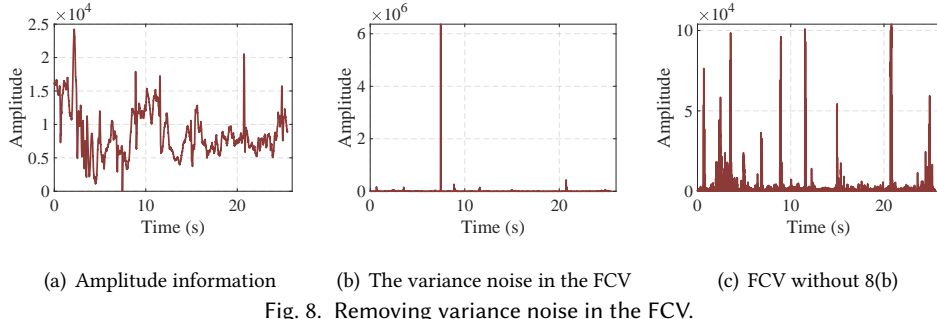


Fig. 8. Removing variance noise in the FCV.

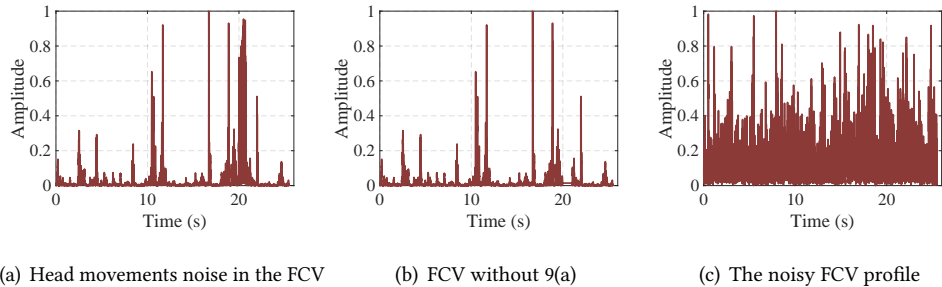


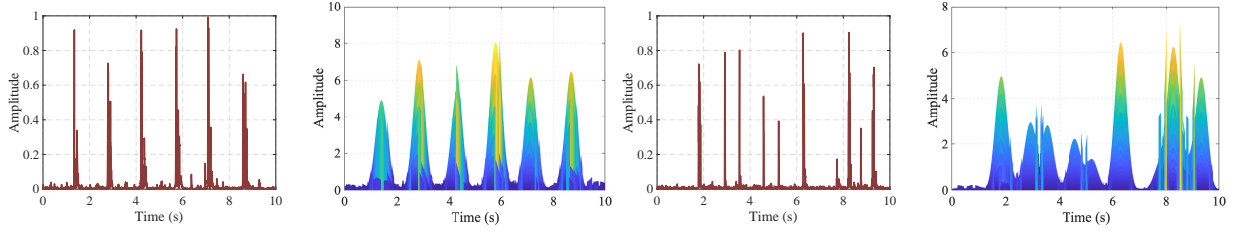
Fig. 9. Eliminating head movements and devices noises.

this disturbance if the peak number is greater than 10, which indicates the presence of huge motion, such as head movement. This is because the execution of 10 blinks within 312.32ms is highly unlikely for a human to accomplish. As demonstrated in Fig. 9(b), we can effectively eliminate the interference introduced by head movements.

As shown in Fig. 9(c), it can be observed that, in addition to the variance noise in FCV and noise induced by head movements, there is also noise from the device, such as data packet loss, that can blend in with the signals. This noise can cause the FCV profile to appear messy. The key to this noise removal lies in determining when the signal becomes distorted. Empirically, we have observed that the median(FCV) of blinks does not exceed 0.05 within 10 seconds. Therefore, to address this issue, we use a sliding window of 10 seconds to identify and remove the messy FCV profiles based on the criterion that $\text{median}(\text{FCV}) \geq 0.05$.

3.4.2 Extracting DED Biomarkers. Given the FCV profile, we aim to extract the DED pattern from the profile to capture the features of dry eye disease, which contains biomarkers of DED. Spontaneous blinking is a non-stationary signal that is sparsity and aperiodicity. Time-domain signals may reveal some characteristics of spontaneous blinking, but they lack portrayal of spontaneous blink motions. Frequency domain analysis can transfer the signal to the frequency domain to reveal frequency domain characteristics, such as the Fast Fourier transform (FFT). However, FFT can only analyze the overall frequency domain characteristics of the signal and cannot represent local features, which are crucial for extracting DED patterns.

To address this issue, we use the Fourier synchrosqueezed transform (FSST) method [10, 26], which combines time-domain and frequency-domain analysis simultaneously. FSST can extract DED features that reflect the frequency content and law of the frequency content changing with time of the spontaneous blinking signal. FSST achieves higher time and frequency resolution compared to the windowed STFT and generates sharper



(a) Spontaneous blinking in a normal person (b) Extracted feature from 10(a) (c) Spontaneous blinking in a DED patient (d) Extracted feature from 10(c)

Fig. 10. The pattern extraction of dry eye disease from spontaneous blink action.

time-frequency estimates. Therefore, for a given FCV profile $f(x)$, the FSST computes:

$$f_1(t, \eta) = \int_{-\infty}^{\infty} f(x)g(x-t)e^{-j2\pi\eta x+j2\pi\eta t}dx \quad (8)$$

where g denotes a spectral window, $e^{j2\pi\eta t}$ denotes an extra factor. The transformed values $f_1(t, \eta)$ have the ability to converge around curves of instantaneous frequency in the time-frequency domain, resulting in higher resolution for both time and frequency when compared to the windowed STFT. Therefore, the FSST can be denoted as:

$$f_2(t, \omega) = \int_{-\infty}^{\infty} f_1(t, \eta)\delta(\omega - \omega_{if})d\eta \quad (9)$$

where $\omega_{if} = \frac{1}{j2\pi} \frac{\frac{\partial}{\partial t} f_1(t, \eta)}{f_1(t, \eta)}$ denotes the estimated instantaneous frequencies. The time-frequency spectrum in Eq. 9 captures biomarkers of dry eye disease. As shown in Fig. 10(b) and Fig. 10(d), the signal profile of a normal person is conspicuously different from that of a DED patient. The extraction of a clear and distinct signal profile is essential for accurate early screening dry eye disease.

3.5 Deep Learning-based DED Screening

Given the extracted DED features, we develop a deep learning-based framework with the ability of DED early screening for a new user. We expand on this idea, providing details of the three key components, i.e., extracting representation of DED biomarkers, global and local unsupervised domain adaptation, and class balancing.

3.5.1 Extracting Representation of DED Biomarkers. To accurately screen for DED, it is important to extract representations of its biomarkers contained in the extracted DED pattern from the profile, such as incomplete blinking frequency, partial blinks, short blink intervals, and prolonged eyelid closed time. As shown in Fig. 2, DED biomarkers, such as maximum inter-blink interval, incomplete blinking frequency, and prolonged eyelid closed time, exhibit temporal characteristics. Therefore, the key issue is how to extract long-term dependencies in the extracted DED pattern from the profile. To achieve this goal, we leverage Multi-head Self-Attention (MSA) [35] to capture long-range dependencies in the time domain and focus on crucial biomarkers.

To align with the 2D data format of extracted DED pattern from the profile, we utilize ViT-based [15] methods to model long-range dependencies among DED biomarkers across the entire DED pattern. However, ViT-based [15] methods rely on large-scale pre-training and global context modeling to enhance its performance. As we employ the pre-trained ViT and fine-tune it for DED screening, we maintain the same patch size, resulting in a longer effective sequence length. Therefore, we reshape the feature $x \in \mathbb{R}^{H \times W \times C}$ into flattened 2D patches $x_p \in \mathbb{R}^{N \times (P^2 \cdot C)}$, where (H, W, C) the input feature's resolution and number of channels, and (P, P) denotes the

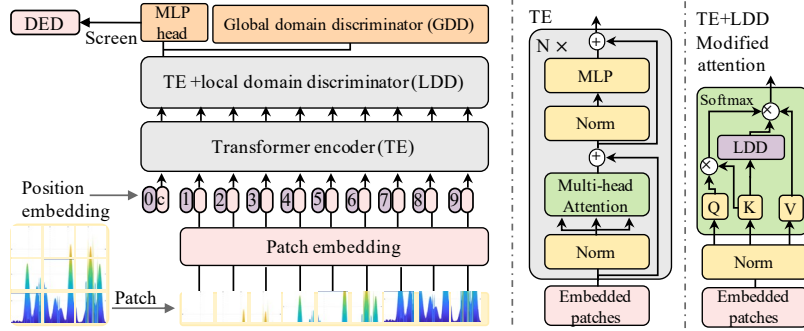


Fig. 11. Deep learning-based framework of DED screening.

resolution of each patch. $N_p = \frac{H}{P} \cdot \frac{H}{P}$ denotes the number of patches for each input feature. We conduct patch embedding to map these flattened patches to D dimensions using a trainable linear projection. To preserve timing information in the feature, we add position embedding to the patch embeddings. Before putting these embedded patches into the transformer endcoder (TE), we prepend a learnable class token x_{class} to serve as a screening representation for DED. We set $N_b = 11$ for the TE block to extract the representation of DED biomarkers.

3.5.2 Adapting to New Users. To empower SDE the ability to adapt a new user, we incorporate UDA [41] to mitigate the influence of variations in both user and environmental factors. As depicted in Fig. 11, our approach includes two domain discriminators, operating at global and local scopes.

For local UDA, we use a patch-level domain discriminator [38] to match features of each patch in different domains by optimizing:

$$\mathcal{L}_p(x^s, x^t) = -\frac{1}{nJ} \sum_{x_i \in \mathcal{D}} \sum_{j=1}^J \mathcal{L}_{ce}\left(D_p\left(G_f(x_{ij}^{\vee})\right), y_{ij}^d\right), \quad (10)$$

where n and J represent the number of samples and patches, \vee denotes either the source s or the target t domain, $G_f(x_{ij})$ and $D_p(\cdot)$ denote learned feature and domain probability of each token, respectively. $G_f(x_{ij})$ learns domain-invariant features in each patch to deceive $D_p(\cdot)$, whereas $D_p(\cdot)$ distinguishes whether features are from the source-domain or target-domain. The local domain discriminator is baked into a transformer endcoder by modifying the self-attention mechanism in the MSA. Specifically, the modified self-attention can be denoted as $SA(Q, K, V) = softmax((Q_c K^T) / (\sqrt{d}) * Concat(1, h(D_p(K))V))$, where Q_c , K , V , and d denote a query of the class patch token, a key and a value of each patch token, and a dimension of K , $*$, $Concat$, and $h(\cdot)$ denote multiplying corresponding elements, concatenation operation, standard entropy function, respectively. By implementing local UDA, we can eliminate the interference of users and environments in fine-grained representations of DED biomarkers.

For global UDA, we introduce a screening representation discriminator that matches the features of the class token across different domains. This is achieved by optimizing the following objective:

$$\mathcal{L}_g(x^{\vee}, y^s) = \sum_{x_i \in \mathcal{D}_s} \frac{\mathcal{L}_{ce}(G_c(f_i^s), y_i^s)}{n_s} - \sum_{x_i \in \mathcal{D}} \frac{\mathcal{L}_{ce}(D_g(f_i^{\vee}), y_i^d)}{n_{s+t}}, \quad (11)$$

where $D = D_s + D_t$, \mathcal{L}_{ce} , d , and f_i denote the datasets, the cross-entropy loss, domain label, and learned global feature in the class tokens, respectively. G_c and D_g denote the classifier for early screening and discriminator for domain identifying. Hence, by minimizing and maximizing in both the global and local scopes, which removes



Fig. 12. Device.

Fig. 13. Eye examination room.

Fig. 14. Clinic.

Fig. 15. Office.

Fig. 16. Home.

interference from different users and environments in both local and global feature spaces, *SDE* acquires the capability to adapt to a new user.

Towards efficiently removing the impact of different users and environments, it is desirable to minimize the empirical risk of DED screening on a new user. However, using two levels of domain discriminator may destroy the biomarker information in the class token. To retain the biomarker representation in the feature space, we leverage the semantic constraints of a new user. Specifically, we aim to ensure that $BI^t = \text{softmax}(G_c(f_i^t))$ contains as much biomarker information about a new user as possible [28]. Additionally, the decision boundary of *SDE* should lie in low density regions [12]. According to mutual information of distribution between a new user and its screening results, we can satisfy the semantic constraints by maximize the mutual information $I(BI^t; x^t) = H(\overline{BI^t}) - \frac{1}{n_t} \sum_{k=1}^{n_t} h(BI_k^t)$, where $K = 2$, $\overline{BI^t} = \mathbb{E}_{x_t}[BI^t]$ is expected value of BI^t over the distribution of x_t .

3.5.3 Balancing Classes and Screening DED. To address the issue of unbalanced data samples in each class, where the number of normal people is much larger than that of dry eye patients, we introduce a punishment mechanism to mitigate the impact of this class imbalance. If normal people has too many data than dry eye patients, the class of normal people tends to dominate the loss and gradient, making it easier to be classified [22]. Therefore, to balance the importance of each class, we add focal loss to down-weight the class with large dataset sizes, forcing the model pay equal attention to each class. The focal loss function is defined as $FL(p_t) = -\alpha_t(1-p_t)^\gamma \log(p_t)$, where $(1-p_t)^\gamma$ and p_t denote a modulating factor and model prediction result of each class, and α_t and γ are hyper-parameters.

To add inductive bias for the transformer, we use ViT with a 16×16 patch size [16] pre-trained on ImageNet-21K [14] as our backbone. We give out the objective function of *SDE* for DED early screening as $\mathcal{L}_g(x^v, y^s) + \mathcal{L}_p(x^s, x^t) + I(BI^t; x^t) + FL(p_t)$.

4 EVALUATION

We conduct a series of extensive experiments¹ to evaluate the effectiveness of *SDE* in realistic environments, which aim to answer the following questions.

- (Q1) Does *SDE* accurately screen for DED?
- (Q2) Does the design of *SDE* benefits to its effectiveness in early screening?
- (Q3) Is *SDE* effective and robust under different settings?

4.1 Experiment Setup

Without modifications on both software and hardware, we realize a prototype of *SDE* with a COTS radar [2], as shown in Fig. 12. Our algorithms are implemented using Matlab 2019b, Python 3, and Pytorch 1.8.

¹Our experiments are approved by both the Ethics Committee of our institutions and the cooperative hospital.

We have recruited 54 participants (25 females and 29 males) aged between 19 to 87, with heights ranging from 150cm to 180cm, which included 27 DED patients and 27 normal people. We recruited participants from two places, i.e., hospitals and schools. They are diagnosed by professional doctors or clinicians in a hospital. The DED cases meet the following criteria: (i) one of the subjective symptoms such as dryness, foreign body sensation, burning sensation, fatigue, discomfort, and vision fluctuations and tear film breakup time; (ii) $UT \leq 5\text{s}$ or Schirmer I test (no topical anesthesia) $\leq 5\text{mm}/5\text{min}$; (iii) one of the subjective symptoms such as dryness, foreign body sensation, burning sensation, fatigue, discomfort, and vision fluctuations and $5\text{s} \leq BUT \leq 10\text{s}$ or $5\text{mm}/5\text{min} \leq$ Schirmer I test results (No topical anesthesia) $\leq 10\text{ mm}/5\text{min}$, corneal and conjunctival fluorescein staining is positive. At the same time, healthy people meet the following criteria: (i) no systemic diseases such as diabetes, hypertension, etc.; (ii) best corrected visual acuity BCVA ≥ 1.0 ; (iii) absence of eye disease; In addition, the exclusion criteria includes: (i) keratitis, conjunctivitis, trichiasis, ties; (ii) those who withdrew from the study midway through the trial. (iii) patients who cannot perform eye blinking due to various factors. As shown in Figs. 13, 14, 15, and 16, we conducted experiments in four realistic and practical scenarios, i.e., eye examination room, clinic, office, and home. Specifically, the eye examination room and clinic room are located in a hospital, and the collected data of the study is in the pipe line of the patient's other examination. In the ophthalmology clinic room, doctors provide diagnostic services for patients with eye diseases. In the ophthalmic examination room, doctors provide various examinations and tests for patients, e.g., tear film breakup time, tear river height, meibomian gland infrared imaging. For each user, it only needs five minutes to perform during the study. In total, we collect over 247,001 samples from the 54 participants for evaluation. The samples are labeled according to both DED patients and normal people. In default settings, we set the distance between the device and a user to 30cm , both the horizontal and vertical angles between the device and a user to 0° , and a user sits in front of the device without performing any specific task.

Model training. To generate an effective and resilient model, our training dataset contains of two parts, i.e., labeled data $D_s = (X_i, Y_i)$ and unlabeled data $D_t = (X_j)$.

The evaluation metrics are defined as follows.

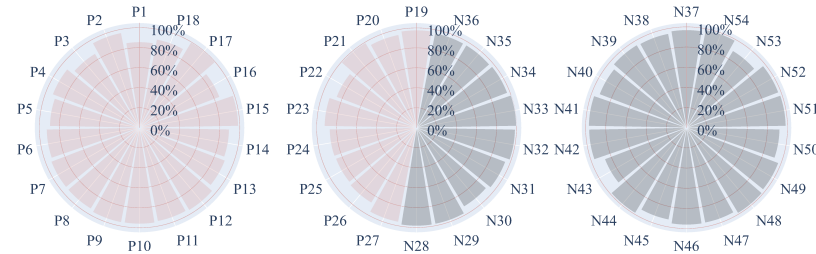
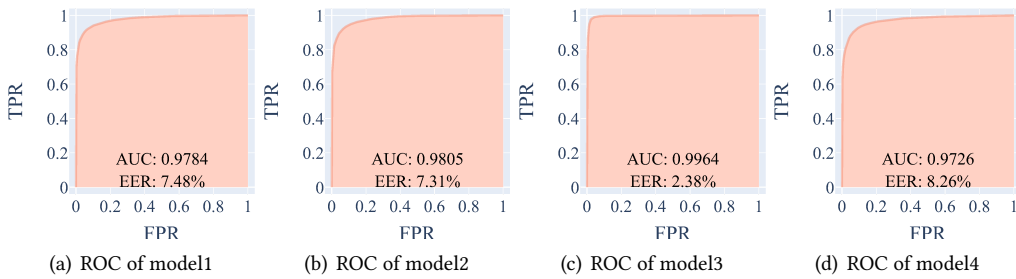
- **Basic Accuracy Metrics:** Accuracy refers to the ratio of the number of correctly classified samples to the total number of samples. Precision indicates the accuracy of the DED predictions made by *SDE*. Recall denotes the ability of *SDE* to correctly identify DED samples. F1-score provides a balanced measure of *SDE* based on the weighted harmonic average of precision and recall.

- **Error Analysis Metrics:** False alarm rate (FAR) is the probability of misclassifying a sample of a normal person as a DED patient. Missing alarm rate (MAR) denotes the probability of misclassifying a sample of a DED patient as a normal person. Equal error rate (EER) is the point where the false negative rate is equal to the false positive rate.

- **Receiver Operating Characteristic (ROC) Metrics:** ROC plots the true positive rate (TPR) against the false positive rate (FPR) at different thresholds, representing the trade-offs between sensitivity and specificity. Area under the curve (AUC) denotes the ability of *SDE* to distinguish between DED patients and normal people.

4.2 Overall Performance

To answer the question (**Q1**), we empirically evaluate the effectiveness of *SDE* in four realistic environments. Specifically, we split all participants into training and test datasets under 3-fold cross-validation methods. In addition, we put 50% unlabeled data $D_t = (X_j)$ from the target test user into the training dataset to eliminate the interference caused by different users and environments. It serves as a fine-tuning process when a new user utilizes *SDE*. Specifically, the new user only needs to sit in front of *SDE* for a while (e.g., 5min), and *SDE* automatically conducts model fine-tuning using the collected data. It should be noted that the data used for

Fig. 17. The screening accuracy of *SDE* among different users.Fig. 18. The receiver operating characteristic curve of four models of *SDE*.

fine-tuning the model does not require labels. After the model is fine-tuned, *SDE* can conduct early screening for the new user. Subsequently, *SDE* becomes capable of facilitating pervasive early screening for DED in daily life.

We evaluate the effectiveness of *SDE* for the 54 users under four realistic scenarios and show the results in Fig. 17. It can be found that *SDE* achieves an average accuracy of 94.22% for DED screening. As shown in Fig. 18, we randomly select four models to evaluate the metrics of ROC under different scenarios, namely the eye examination room, clinic, office, and home. It is evident that the ROC curves are close to the top left corner of the plot, indicating high TPR and low FPR for all thresholds. The AUCs for the four models are 0.9784, 0.9805, 0.9964, and 0.9726, and, the EERs are 7.84%, 7.31%, 2.38%, and 8.26%, respectively. Model3 has a lower EER than the others because the target test users are mainly from the office scenario, which reduces the interference from different environments. As shown in Fig. 19, we demonstrate the models' performance of *SDE* with three metrics, i.e., precision, recall, and F1-score. It can be observed that the models achieve above 91.43% for these three metrics. As shown in Fig. 20, the FAR and MAR of the models are lower than 8.51%. These represent that *SDE* can accurately screen DED.

We also analyze the time cost of calculations for *SDE*, which includes the entire data processing and model prediction as discussed in Section 3. For each sample, the total calculation time is no more than 2.37s. This demonstrates that *SDE* has the potential to screen DED in real-time.

4.3 Ablation Study

To answer the question (Q2), we empirically evaluate the effectiveness of *SDE* in three impact factors, i.e., FCV construction, threshold of noise filtering, and DED biomarker.

4.3.1 Evaluation of FCV Construction. Different numbers of frame chirps used in the construction of the FCV can affect the noise introduced and subsequently impact the detection of spontaneous blinking, which in turn can influence the screening of DED. To evaluate the effectiveness of *SDE* under different FCV settings, we conducted empirical tests using varying numbers of chirps.

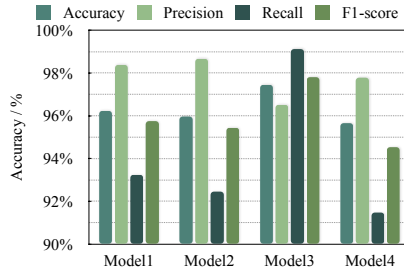


Fig. 19. The basic accuracy metrics of four random models.

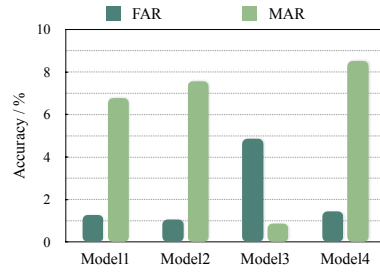


Fig. 20. The FAR and MAR of four random models.

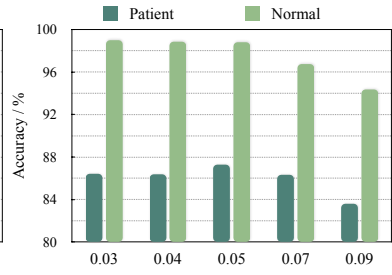


Fig. 21. Impact of thresholds.

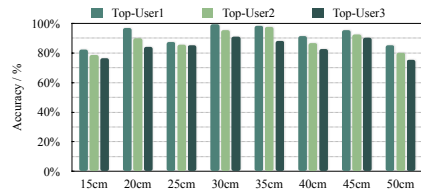


Fig. 22. Impact of distances.

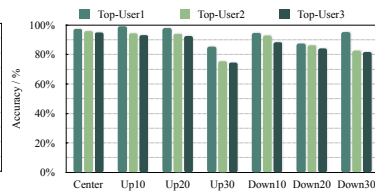


Fig. 23. Impact of vertical angles.

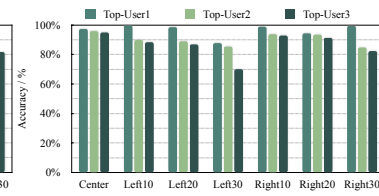


Fig. 24. Impact of horizontal angles.

As shown in Fig. 25, the average screening accuracy of SDE is respectively 78.9%, 81.53%, 93%, 82.56%, 76.12%, and 73.47% with the chirp number to be 8, 24, 32, 40, 48, and 64 in Eq. 5. The screening accuracy of 16 and 32 chirp numbers are similar, while 64 has the lowest screening accuracy. The reason is that FCV with a longer time frame will lose perception of spontaneous blinking, whereas FCV with less time will be too sensitive to background noises. Therefore, there is a trade-off between the number of chirps and FCV perception. We choose 32 chirps as a default setting.

4.3.2 Evaluation of Threshold of Noise Filtering. Since except for the noises of multi-path from realistic environments, there is other noise from the device, i.e., data packet loss, which can also bring noise. We utilize a threshold to filter out noise filtering, bringing decrease in the amount of data. Therefore, we empirically evaluate the effectiveness of SDE under different threshold levels.

As shown in Fig. 21, the average screen accuracy of SDE are respectively 92.69%, 92.63%, 93.95%, 91.55%, and 88.98% with the threshold to be 0.03, 0.04, 0.05, 0.07, and 0.09. The screening accuracy of 0.03 and 0.04 threshold are similar, while 0.09 has the lowest screening accuracy. The reason is that threshold value affects the quality of spontaneous blinking signal by controlling the amount of noise in the data.

Specifically, the data with a threshold of 0.03 has higher quality than that of 0.04, which has bigger dataset sizes than that of 0.03. However, when the threshold falls to 0.09, the accuracy of SDE declines to 88.98% since more noise is introduced as the amount of data increases. We choose a default threshold value of 0.05 as it provides a balance between signal cleanliness and dataset size.

4.3.3 Evaluation of DED Biomarker. Based on FCV, we extract the DED pattern from the profile of spontaneous blink dynamics. Following this, we utilize Multi-head Self-Attention (MSA) to capture DED biomarkers such as incomplete blinking frequency, partial blinks, short blink intervals, and prolonged eyelid closed time. However, it remains unclear whether the biomarkers mentioned in Section 2.3 help with DED early screening. To empirically evaluate this issue, we conduct a comparative experiment of DED early screening with specific biomarkers, such as maximum inter-blink interval (MBI) [20] [34]. To extract the MBI, we evaluate the interval of each blink (as shown in Fig. 10) and retain the two blinks with the longest inter-blink interval, setting the other blink signals

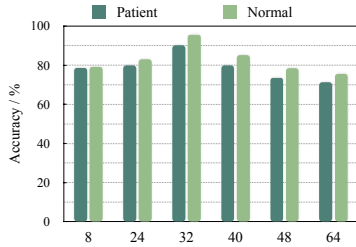


Fig. 25. Impact of FCV construction.

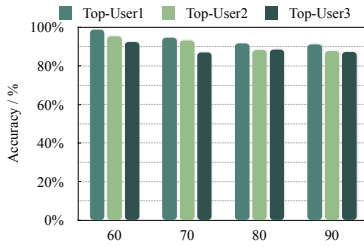


Fig. 26. Impact of chirp duration.

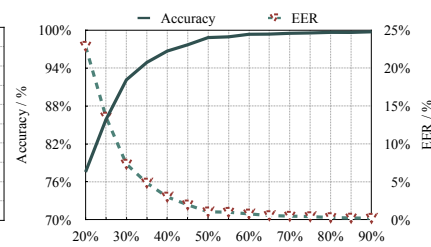


Fig. 27. Impact of dataset size.

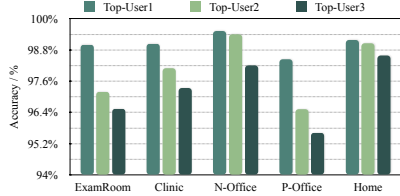


Fig. 28. Impact of scenes.

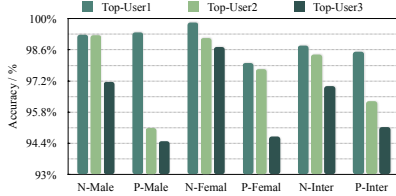


Fig. 29. Impact of genders.

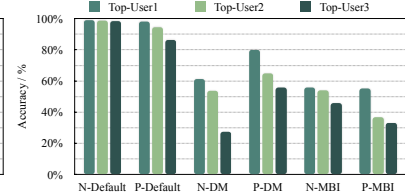


Fig. 30. Comparison of biomarkers.

to 0. Specifically, we test 10 participants (5 normal, and 5 DED patients) under three settings, i.e., both training and testing on DED pattern (N/P-Default), train on DED pattern and test on DED pattern with MBI extracted (N/P-DM), and both training and testing on DED pattern with MBI extracted (N/P-MBI).

As shown in Fig. 30, the average screening accuracy is 95.79%, 57.12%, and 46.81% for the three settings of N/P-Default, N/P-DM, and N/P-MBI, respectively. This indicates that biomarkers extracted by *SDE* outperform the MBI biomarker. It can be seen that the highest accuracy in the N/P-DM is 79.92%, indicating that *SDE* can also capture the MBI. The low screening accuracy in the N/P-MBI setting suggests that a single MBI biomarker is insufficient for DED screening.

4.4 Robustness

To answer the question (Q3), we empirically evaluate the effectiveness of *SDE* under different settings, i.e., chirp duration, scenarios, angles, distances, and training set sizes.

4.4.1 Impact of Chirp Duration. We empirically evaluate the effectiveness of *SDE* with different chirp durations settings, i.e., 60us, 70ms, 80us, and 90us. For each kind of setting, we select 3 normal people as test datasets, and the rest of the users as training datasets.

Fig. 26 demonstrates that the effectiveness of *SDE* decreases as the chirp durations increases. The average accuracy of DED screening is 95.50%, 91.57%, 89.37%, and 88.71% with the chirp durations to be 60us, 70us, 80us, and 90us, respectively. It can be seen that *SDE* achieves the highest average accuracy with 60us chirp durations. This is because the chirp duration affects the granularity of RF signals in *SDE*, and lower chirp durations can capture more specific information about spontaneous blink actions.

4.4.2 Impact of Angles. We empirically evaluate the effectiveness of *SDE* under different angles between users and radio device. These angles included vertical up angles of 0°, 10°, 20°, and 30°, vertical down angles of 10°, 20°, and 30°, horizontal left angles of 10°, 20°, and 30°, and horizontal right angles of 10°, 20°, and 30°. For each kind of angle, we select 3 normal individuals as test datasets, and the rest of the users as training datasets.

As shown in Fig. 23, the performance of *SDE* degrades as the angle between the user and radio device increases in both upward and downward directions. For downward angles of 10°, 20°, and 30°, the average screening accuracy of *SDE* is 91.94%, 85.96%, and 86.51%, respectively. Similarly, for upward angles of 0°, 10°, 20°, and 30°,

the average screening accuracy of *SDE* is 96.03%, 95.58%, 94.73%, and 78.45%, respectively. It is evident that *SDE* performs best when the angle is 0° because RF signals can ideally be bounced off a user's eyes.

Fig. 24 shows that the effectiveness of *SDE* decreases as the horizontal angle between the user and radio device increases in both leftward and rightward directions. For leftward angles of 10°, 20°, and 30°, the average screening accuracy of *SDE* is 92.61%, 91.48%, and 81.03%, respectively. Similarly, for rightward angles of 0°, 10°, 20°, and 30°, the average screening accuracy of *SDE* is 96.03%, 95.12%, 93.06%, and 88.8%, respectively. It is evident that *SDE* achieves the highest average accuracy when the angle is 0°. However, *SDE* has different performance among leftward and rightward direction. This is because RF signals can mainly be bounced off one eye of a user (i.e., left or right eye) when the horizontal angle increases.

4.4.3 Impact of Distances. We empirically evaluate the effectiveness of *SDE* with different chirp durations, specifically 15cm, 20cm, 25cm, 30cm, 35cm, 40cm, 45cm, and 50cm. For each kind of setting, we select 3 normal individuals as test datasets, and the rest of the users as training datasets.

As shown in Fig. 22, the average screening accuracy of *SDE* is 79.1%, 90.36%, 86.03%, 95.3%, 94.72%, 86.98%, 92.8%, and 80.35% for the distance of 15cm, 20cm, 25cm, 30cm, 35cm, 40cm, 45cm, and 50cm, respectively. It can be seen that the performance of *SDE* at a distance of 50 is close to the lowest performance. This is because the RF signal at this distance has the strongest influence of multi-path from realistic environments. The lower performance of *SDE* at a distance of 15cm is attributed to susceptibility to interference from direct path signals in this range. Therefore, we use 30cm as the default choice.

4.4.4 Impact of Different Scenes. We empirically evaluate the effectiveness of *SDE* with different scenes, i.e., eye examination room, clinic, office, and home. The eye examination room and clinic had only patients as participants, while the home scene only had normal individuals. The office scenes consisted of both normal individuals and patients. We selected three individuals in each class of every scene as test datasets, and the rest of the users as training datasets.

As shown in Fig. 28, the average screening accuracy of *SDE* is 97.58%, 98.16%, 97.95%, and 98.94% for the scenes of eye examination room, clinic, office, and home, respectively. *SDE* has similar performance under four scenes, indicating that it could effectively remove the noise from realistic environments, especially in the eye examination room where patients are lined up for eye tests.

4.4.5 Impact of Training Dataset Size. We empirically evaluate the effectiveness of *SDE* with different dataset size. As discussed in Section 4.3.2, there is a trade-off between signal cleanliness and dataset size when setting the threshold. Therefore, we investigate the effectiveness of *SDE* with varying proportions of data from each participant for training. Specifically, we split all participants into training and test datasets under 3-fold cross-validation methods. For each participant in the training datasets, we randomly select different proportions of data for training.

As shown in Fig. 27, there is a clear relationship between the screening performance of *SDE* and the size of the training dataset. The EER decreases as the dataset size increases, and the effectiveness of *SDE* reaches a saturation point at 50% of the data from each participant. According to Section 4.1 and 4.3.2, *SDE* contains sufficient training datasets to reach the saturated point, ensuring DED screening with high accuracy.

4.4.6 Impact of Genders. We empirically evaluate the effectiveness of *SDE* with different genders, namely male, femal, intergender. For each gender class, we select 5 individuals as test datasets, and the rest of the users as training datasets.

As presented in Fig. 29, the average screening accuracy of *SDE* is 97.45%, 98.02%, and 97.35% for the gender of male, femal, and intergender, respectively. It can be seen that *SDE* performs similarly well across different genders. This is due to the fact that *SDE* captures the spontaneous blink movement, which can indicate abnormalities in the eyes regardless of gender.

5 RELATED WORK

5.1 Clinical Diagnosis for Dry Eye Disease

In 2017, the Dry Eye Workshop of TFOS released a diagnostic methodology report [39], indicating that numerous clinical tests could be utilized for diagnosing dry eye disease. However, since many consider DED to be a symptom-based disease, symptom assessment is a critical aspect of diagnosis. Several questionnaires, such as the ocular surface disease index [29] and McMonnies & Ho dry eye questionnaire [17], can be used to determine a score for diagnosis. The slit lamp examination is used for documenting eye damage and conducting DED assessment.

Schirmer's test measures the amount of tears by placing a filter paper into the junction of the middle and outer 1/3 of the conjunctival sac under the tested eye. If more than 10 mm of moisture is on the test paper in 5 minutes, then the result is negative[32]. Tear break-up time measures the time it takes for the first dry spot to arise on the cornea after a fine-grained blink [7]. Meibomian gland analysis measures the function of meibomian gland abnormalities, which secrete meibum oil [9], [30]. Tear osmolarity measures tear salt content, where hyperosmolarity indicates high salt concentration and is strongly associated with DED [11]. Tear river height measures the level of tear fluid at the junction of the light band on the corneoconjunctival surface and the lower eyelid margin light band, representing tear secretion [24].

However, these clinical diagnoses have certain problems, such as high detection costs, in-hospital designated testing, and intrusive inspection. Therefore, it is essential to develop a dry eye screening system that is convenient, universal, and suitable for home monitoring, benefiting for early detection and timely intervention.

5.2 Camera Based Dry Eye Disease Screening

Yedidya et al. [43] proposed an automated DED detection method based on analyzing dry areas in videos after introducing fluorescein into the tear film. Su et al. [33] presented a contactless DED detection method that measures variations in ocular surface temperature during a 6s eye-open period, using a specially designed contactless infrared thermal imaging system. Vyas et al. [36] proposed a computer-aided diagnosis method for DED that utilizes deep neural networks to detect the tear film breakup time based on TBUT, helping ophthalmologists in prescribing treatments. However, these methods require extra operations [43], specific hardware [33], and in-hospital medical equipment [36]. Acharya et al. [8] proposed a contactless DED detection method that can identify between normal and DED based on infrared thermography images. However, the infrared camera costs \$60,000. Hong et al. [19] proposed a contactless DED detection method that captures images of the eyes using a smartphone, achieving 75% accuracy for minor DED identifying. Although this method uses a ubiquitous device, i.e., smartphone, the detection performance is only 75%. And, they proposed a DED detection method that measures the height of the tear meniscus using a smartphone and a small, portable LED ring-light [18]. SDE utilizes RF to capture the spontaneous blink dynamics, which eliminates concerns about lightness disturbance and privacy associated with vision-based methods.

5.3 RF Based Application

Wireless signals are becoming popular due to their contactless and ubiquitous nature, resulting in numerous RF-based applications in both industry [3, 4] and academia [23, 37, 40, 42, 44, 46] in recent years.

Google Nest Hub (2nd gen) [3] uses Soli radar chip [4] to conduct sleep sensing, providing personalized tips to improve the users' sleep and overall health. Zheng et al. [46] monitor drivers' vital signs using an FMCW radar device. Zhao et al. [44] use RF signals to facilitate monitoring medication self-administration. Wang et al. [37] use mmWave radar to eavesdrop on a smartphone's earpiece. Yang et al. [42] propose an assessment method for diagnosing and tracking the progression of Parkinson's disease based on nocturnal breathing, extracted from wireless signals. Xue et al. [40] monitor diaper wetness using a mmWave radar. Liu et al. [23] propose gait as a marker for Parkinson's disease progression, severity, and medication response through an FMCW radio device.

In our work, we construct FCV from RF signals to capture fine-grained spontaneous blinking and extract DED biomarker representations, realizing a contactless, convenient, and ubiquitous DED screening system.

6 CONCLUSION

In this paper, we propose *SDE*, a contactless, convenient, and ubiquitous DED screening system based on RF signals. We construct a frame chirps variance that captures fine-grained spontaneous blinking. To render a practical system, we design a series algorithms to remove entwined non-linear interference in the frame chirps variance. Based on the characterization of spontaneous blinking, we extract representation of DED biomarkers that denote the symptoms of DED. We develop a deep learning-based framework that leverages both global and local unsupervised domain adaptation to endow *SDE* with the ability to adapting to new users. We validate *SDE* through extensive experiments and confirm its generalisability and effectiveness. We believe *SDE* can serve as a practical DED early screening system, enabling early diagnosis, timely intervention and benefitting high-risk susceptible populations.

ACKNOWLEDGMENTS

We thank the anonymous reviewers for their constructive comments. This research is supported in part by RGC under Contract CERG 16204820, 16206122, AoE/E-601/22-R, Contract R8015, and 3030_006.

REFERENCES

- [1] 2021. DCA1000EVM. <https://www.ti.com/tool/DCA1000EVM>.
- [2] 2021. IWR1443BOOST. <https://www.ti.com/tool/IWR1443BOOST>.
- [3] 2022. Nest Hub (2nd gen). https://store.google.com/us/product/nest_hub_2nd_gen?hl=en-US.
- [4] 2022. Soli. <https://atap.google.com/soli/>.
- [5] 2023. Dry Eye Syndrome. https://eyewiki.aao.org/Dry_Eye_Syndrome.
- [6] 2023. EYE BLINK SENSING SYSTEM - WORKING PRINCIPLE. <https://robocraze.com/blogs/post/eye-blink-sensing-system-working-principle>.
- [7] Mark B Abelson, George W Ousler, Lauren A Nally, Donna Welch, and Kathleen Krenzer. 2002. Alternative reference values for tear film break up time in normal and dry eye populations. In *Lacrimal Gland, Tear Film, and Dry Eye Syndromes 3*. Springer, 1121–1125.
- [8] U Rajendra Acharya, Jen Hong Tan, Joel EW Koh, Vidya K Sudarshan, Sharon Yeo, Cheah Loon Too, Chua Kuang Chua, EYK Ng, and Louis Tong. 2015. Automated diagnosis of dry eye using infrared thermography images. *Infrared Physics & Technology* 71 (2015), 263–271.
- [9] Reiko Arita, Jun Suehiro, Tsuyoshi Haraguchi, Rika Shirakawa, Hideaki Tokoro, and Shiro Amano. 2014. Objective image analysis of the meibomian gland area. *British Journal of Ophthalmology* 98, 6 (2014), 746–755.
- [10] François Auger, Patrick Flandrin, Yu-Ting Lin, Stephen McLaughlin, Sylvain Meignen, Thomas Oberlin, and Hau-Tieng Wu. 2013. Time-frequency reassignment and synchrosqueezing: An overview. *Signal Processing Magazine* 30, 6 (2013), 32–41.
- [11] Umberto Benelli, Marco Nardi, Chiara Posarelli, and Timothy G Albert. 2010. Tear osmolarity measurement using the TearLab™ Osmolarity System in the assessment of dry eye treatment effectiveness. *Contact Lens and Anterior Eye* 33, 2 (2010), 61–67.
- [12] Olivier Chapelle and Alexander Zien. 2005. Semi-supervised classification by low density separation. In *International workshop on artificial intelligence and statistics*. PMLR, 57–64.
- [13] Michael Chau and Margrit Betke. 2005. *Real time eye tracking and blink detection with usb cameras*. Technical Report. Boston University Computer Science Department.
- [14] Jia Deng, Wei Dong, Richard Socher, Li-Jia Li, Kai Li, and Li Fei-Fei. 2009. Imagenet: A large-scale hierarchical image database. In *Conference on computer vision and pattern recognition*. IEEE, 248–255.
- [15] Alexey Dosovitskiy, Lucas Beyer, Alexander Kolesnikov, Dirk Weissenborn, Xiaohua Zhai, Thomas Unterthiner, Mostafa Dehghani, Matthias Minderer, Georg Heigold, Sylvain Gelly, et al. 2020. An image is worth 16x16 words: Transformers for image recognition at scale. *arXiv preprint arXiv:2010.11929* (2020).
- [16] Alexey Dosovitskiy, Lucas Beyer, Alexander Kolesnikov, Dirk Weissenborn, Xiaohua Zhai, Thomas Unterthiner, Mostafa Dehghani, Matthias Minderer, Georg Heigold, Sylvain Gelly, et al. 2021. An image is worth 16x16 words: Transformers for image recognition at scale. *International Conference on Learning Representations* (2021).
- [17] Yuxin Guo, Rongmei Peng, Kang Feng, and Jing Hong. 2016. Diagnostic performance of McMonnies questionnaire as a screening survey for dry eye: a multicenter analysis. *Journal of ophthalmology* 2016 (2016).

- [18] Yuting Hong and Makoto Hasegawa. 2021. Proposal of Tear Meniscus Measurement for Minor Dry-eye Detection Using Smart-phone Camera and Ring-light. In *International Technical Conference on Circuits/Systems, Computers and Communications (ITC-CSCC)*. IEEE, 1–4.
- [19] Yuting Hong and Makoto Hasegawa. 2021. Study of minor dry-eye detection using smartphone camera based on deep learning. In *International Workshop on Advanced Imaging Technology (IWAIT)*, Vol. 11766. SPIE, 621–626.
- [20] Ying Jie, Ruti Sella, Jun Feng, Maria L Gomez, and Natalie A Afshari. 2019. Evaluation of incomplete blinking as a measurement of dry eye disease. *The Ocular Surface* 17, 3 (2019), 440–446.
- [21] Dong Li, Jialin Liu, Sunghoon Ivan Lee, and Jie Xiong. 2022. Lasense: Pushing the limits of fine-grained activity sensing using acoustic signals. *Interactive, Mobile, Wearable and Ubiquitous Technologies* 6, 1 (2022), 1–27.
- [22] Tsung-Yi Lin, Priya Goyal, Ross Girshick, Kaiming He, and Piotr Dollár. 2017. Focal loss for dense object detection. In *IEEE international conference on computer vision*. 2980–2988.
- [23] Yingcheng Liu, Guo Zhang, Christopher G Tarolli, Rumen Hristov, Stella Jensen-Roberts, Emma M Waddell, Taylor L Myers, Meghan E Pawlik, Julia M Soto, Renee M Wilson, et al. 2022. Monitoring gait at home with radio waves in Parkinson’s disease: A marker of severity, progression, and medication response. *Science Translational Medicine* 14, 663 (2022).
- [24] Julia C Mainstone, Adrian S Bruce, and Timothy R Golding. 1996. Tear meniscus measurement in the diagnosis of dry eye. *Current eye research* 15, 6 (1996), 653–661.
- [25] Paul McCann, Alison G Abraham, Adhuna Mukhopadhyay, Kanella Panagiotopoulou, Hongan Chen, Thanitsara Rittiphairoj, Darren G Gregory, Scott G Hauswirth, Cristos Infantides, Riaz Qureshi, et al. 2022. Prevalence and incidence of dry eye and meibomian gland dysfunction in the United States: A systematic review and meta-analysis. *JAMA ophthalmology* (2022).
- [26] Thomas Oberlin, Sylvain Meignen, and Valérie Perrier. 2014. The Fourier-based synchrosqueezing transform. In *International conference on acoustics, speech and signal processing (ICASSP)*. IEEE, 315–319.
- [27] Jan U Prause and Mogens Norn. 1987. Relation between blink frequency and break-up time? *Acta ophthalmologica* 65, 1 (1987), 19–22.
- [28] Kuniaki Saito, Donghyun Kim, Stan Sclaroff, Trevor Darrell, and Kate Saenko. 2019. Semi-supervised domain adaptation via minimax entropy. In *IEEE/CVF international conference on computer vision*. 8050–8058.
- [29] Rhett M Schiffman, Murray Dale Christianson, Gordon Jacobsen, Jan D Hirsch, and Brenda L Reis. 2000. Reliability and validity of the ocular surface disease index. *Archives of ophthalmology* 118, 5 (2000), 615–621.
- [30] Sruthi Srinivasan, Kara Menzies, Luigina Sorbara, and Lyndon Jones. 2012. Infrared imaging of meibomian gland structure using a novel keratograph. *Optometry and Vision Science* 89, 5 (2012), 788–794.
- [31] Fiona Stapleton, Monica Alves, Vatinee Y Bunya, Isabelle Jalbert, Kaevalin Lekhanont, Florence Malet, Kyung-Sun Na, Debra Schaumberg, Miki Uchino, Jelle Vehof, et al. 2017. Tfos dews ii epidemiology report. *The ocular surface* 15, 3 (2017), 334–365.
- [32] Sue Stevens. 2011. Schirmer’s test. *Community eye health* 24, 76 (2011), 45.
- [33] Tai Yuan Su, Chen Kerh Hwa, Po Hsuan Liu, Ming Hong Wu, David O Chang, Po Fang Su, Shu Wen Chang, and Huihua Kenny Chiang. 2011. Noncontact detection of dry eye using a custom designed infrared thermal image system. *Journal of biomedical optics* 16, 4 (2011), 046009–046009.
- [34] Yuandong Su, Qingfeng Liang, Guanyu Su, Ningli Wang, Christophe Baudouin, and Antoine Labb  . 2018. Spontaneous eye blink patterns in dry eye: clinical correlations. *Investigative ophthalmology & visual science* 59, 12 (2018), 5149–5156.
- [35] Ashish Vaswani, Noam Shazeer, Niki Parmar, Jakob Uszkoreit, Llion Jones, Aidan N Gomez, Łukasz Kaiser, and Illia Polosukhin. 2017. Attention is all you need. *Advances in neural information processing systems* 30 (2017).
- [36] Aditi Hareesh Vyas, Mayuri A Mehta, Ketan Koticha, Sharnil Pandya, Mamoun Alazab, and Thippa Reddy Gadekallu. 2022. Tear film breakup time-based dry eye disease detection using convolutional neural network. *Neural Computing and Applications* (2022), 1–19.
- [37] Chao Wang, Feng Lin, Tiantian Liu, Kaidi Zheng, Zhibo Wang, Zhengxiong Li, Ming-Chun Huang, Wenyao Xu, and Kui Ren. 2022. mmEve: eavesdropping on smartphone’s earpiece via COTS mmWave device. In *International Conference on Mobile Computing And Networking*. 338–351.
- [38] Ximei Wang, Liang Li, Weirui Ye, Mingsheng Long, and Jianmin Wang. 2019. Transferable attention for domain adaptation. In *AAAI Conference on Artificial Intelligence*. 5345–5352.
- [39] James S Wolffsohn, Reiko Arita, Robin Chalmers, Ali Djalilian, Murat Dogru, Kathy Dumbleton, Preety K Gupta, Paul Karpecki, Sihem Lazreg, Heiko Pult, et al. 2017. TFOS DEWS II diagnostic methodology report. *The ocular surface* 15, 3 (2017), 539–574.
- [40] Meng Xue, Yanjiao Chen, Xueluan Gong, Jian Zhang, and Chunkai Fan. 2022. Wet-Ra: Monitoring Diapers Wetness with Wireless Signals. *Interactive, Mobile, Wearable and Ubiquitous Technologies* 6, 2 (2022), 1–26.
- [41] Jinyu Yang, Jingjing Liu, Ning Xu, and Junzhou Huang. 2023. Tvt: Transferable vision transformer for unsupervised domain adaptation. In *IEEE/CVF Winter Conference on Applications of Computer Vision*. 520–530.
- [42] Yuzhe Yang, Yuan Yuan, Guo Zhang, Hao Wang, Ying-Cong Chen, Yingcheng Liu, Christopher G Tarolli, Daniel Crepeau, Jan Bokartky, Mithri R Junna, et al. 2022. Artificial intelligence-enabled detection and assessment of Parkinson’s disease using nocturnal breathing signals. *Nature medicine* 28, 10 (2022), 2207–2215.

- [43] Tamir Yedidya, Richard Hartley, Jean-Pierre Guillon, and Yogesan Kanagasingam. 2007. Automatic dry eye detection. In *International Conference on Medical Image Computing and Computer-Assisted Intervention*. Springer, 792–799.
- [44] Mingmin Zhao, Kreshnik Hoti, Hao Wang, Aniruddh Raghu, and Dina Katabi. 2021. Assessment of medication self-administration using artificial intelligence. *Nature medicine* 27, 4 (2021), 727–735.
- [45] Qinxiang Zheng, Lei Wang, Han Wen, Yueping Ren, Shenghai Huang, Furong Bai, Na Li, Jennifer P Craig, Louis Tong, and Wei Chen. 2022. Impact of Incomplete Blinking Analyzed Using a Deep Learning Model With the Keratograph 5M in Dry Eye Disease. *Translational vision science & technology* 11, 3 (2022), 38–38.
- [46] Tianyue Zheng, Zhe Chen, Chao Cai, Jun Luo, and Xu Zhang. 2020. V2iFi: in-Vehicle Vital Sign Monitoring via Compact RF Sensing. *Interactive, Mobile, Wearable and Ubiquitous Technologies* 4, 2 (2020), 1–27.